AIAA JOURNAL
Vol. 48, No. 6, June 2010

Finite Difference Lattice Boltzmann Method for Compressible Thermal Fluids

R. M. C. So,* S. C. Fu,† and R. C. K. Leung‡
Hong Kong Polytechnic University, Kowloon, Hong Kong, People's Republic of China

DOI: 10.2514/1.43257

A finite difference lattice Boltzmann method based on the Bhatnagar–Gross–Krook-type modeled Boltzmann equation is proposed. The method relies on a different lattice equilibrium particle distribution function and the use of a splitting method to solve the modeled lattice Boltzmann equation. The splitting technique permits the boundary conditions for the lattice Boltzmann equation to be set as conveniently as those required for the finite difference solution of the Navier–Stokes equations. It is shown that the compressible Navier–Stokes equation can be recovered fully from this approach; however, the formulation requires the solution of a Poisson equation governing a second-order tensor. Thus constructed, the method has no arbitrary constants. The proposed method is used to simulate thermal Couette flow, aeroacoustics, and shock structures with an extended thermodynamics model. The simulations are carried out using a high-order finite difference scheme with a two-dimensional, nine-velocity lattice. All simulations are performed using a single relaxation time and a set of constants deduced from the derivation. It is found that the finite difference lattice Boltzmann method is able to correctly replicate viscous effects in thermal Couette flows, aeroacoustics, and shock structures. The solutions obtained are identical either to analytical results, or obtained by solving the compressible Navier–Stokes equations using a direct numerical simulation technique.

I. Introduction

THE Bhatnagar–Gross–Krook (BGK) model [1] has long played an important role in the development of kinetic theory-based numerical schemes. This is due to the fact that the derivation of the Euler and/or Navier–Stokes (NS) equations from the BGK-type modeled Boltzmann equation (BGK/BE) can be achieved through the Chapman–Enskog or multiscale expansion with Knudsen number ($Kn \ll 1$) as an expansion parameter [2]. Therefore, the BGK/BE provides an alternative to the NS equations for fluid flows in the continuum regime. Since then, different numerical methods have been proposed for the solution of the BGK/BE. Broadwell [3] introduced a discrete velocity method, which is based on the assumption that the gas particles can be restricted to having a limited number of velocities. The conventional lattice Boltzmann method (LBM), which is a special example of a particular discretization of the discrete Boltzmann equation [4], and the finite difference LBM [5,6] fall into this category. These numerical schemes have recently been developed into a promising alternative to model flow physics compared with the NS equations [7], because the modeled BE is hyperbolic and can be solved locally, explicitly, and efficiently on parallel computers [8,9].

In the early development of conventional LBM, a small Mach number $M \ll 1$ assumption was necessary [7]. This is because nonlinear deviations, which are present in the recovery of the NS equations from the lattice BGK/BE, are proportional to M^2, and they originate from the second-order terms in the Chapman–Enskog expansion. This assumption limits the application to near incompressible flows, and the energy equation plays no part in modeling the flow; thus, the approach is restricted to incompressible isothermal flows [10,11]. Since then, much effort has been made to extend the LBM to compressible thermal fluids [12–14]. To represent compressibility in thermal fluids, multiple particle speeds have to be introduced. However, multiple particle speeds require higher-order isotropy in the particle velocity tensor. Such a set of particle speeds might not fill the lattice nodes, and multiple-speed LBM might introduce instability in the numerical simulation. Remedies have been proposed; e.g., Alexander et al. [12] proposed a thermal LBM with the energy equation included. Later, McNamara and Alder [13] showed that LBM could be used to recover the thermal NS equations by fixing a number of moments of the equilibrium distribution function and thus, relaxing the $M \ll 1$ assumption. However, the thermal LBM still has a few limitations; e.g., the Prandtl number Pr is incorrect, and the ratio of specific heats γ is fixed as $(D+2)/D$, where D is the dimension number, because internal energy e is restricted to the translational mode only for monotonic gas. These two limitations are inherent in the conventional LBM.

Various attempts have been made to remedy the monatomic gas assumption in conventional LBM approaches, and these include the concept of multienergy level to facilitate a flexible γ [15,16], or using an additional distribution function to account for the energy equation [17,18]. An alternative approach to consider, including the rotational degree-of-freedom of the gas particles in a modified definition of the total energy, has recently been put forward [19,20]. This approach leads to a slightly modified Maxwellian distribution for the equilibrium particle distribution function f^{eq}. The same approach has been validated against aeroacoustics [20] and shock-capturing [21] problems. Watari [22] extended the method of [23] to allow variable γ to be set for the fluid under consideration. His extension is based on a definition of the total internal energy e_t as the sum of the translational energy and extra energy. Consequently, he obtained an expression for γ given by $\gamma = (D+n+2)/(D+n)$ where n is the number of extra degrees of freedom. The finite difference LBM based on this proposal is numerically stable and represents an improvement over those recently proposed in [24,25]. Therefore, it is possible to extend the BGK/BE to simulate thermal fluid flows in the subsonic to supersonic range without any numerical instability [22].

To use the conventional LBM to simulate thermal fluid flows, Pr deduced from or specified for the BGK/BE has to be correct. The thermal LBM of [12] yields a $Pr = 0.5$, which is inconsistent with real gas. Chen et al. [14] employed a high-order velocity expansion for f^{eq} to correct the viscous stress and the heat flux; however, details of the parameter's construction were not given. Multiple-speed and dual relaxation rate models [26,27] were proposed to allow Pr variation and, hence, its correct evaluation. However, the resulting numerical scheme is unstable; the proposed stabilization schemes

Received 15 January 2009; revision received 10 December 2009; accepted for publication 20 January 2010.

*Visiting Chair Professor, Department of Building Services Engineering; mmmcso@polyu.edu.hk. Fellow AIAA (Corresponding Author).
†Ph.D. Student, Department of Mechanical Engineering.
‡Assistant Professor, Department of Mechanical Engineering. Senior Member AIAA.

were rather ad hoc and might not be applicable for problems besides those treated in [26,27]. Lallemand and Luo [28] decoupled the shear and energy modes of the linearized evolution operator to improve numerical stability; unfortunately, physical background of the modification was not highlighted.

Another difficulty associated with conventional LBM and the finite difference LBM is the setting of boundary conditions in the numerical simulation; reliable boundary setting methods are limited. Through the simulation of microchannel flows, Lim et al. [29] classified the LBM boundary setting method into two common categories, a heuristic boundary condition (specular model, including the earlier bounceback condition) and an extrapolation scheme. According to their heuristic model, momentum is deposited on the wall; arguments and physical meaning of the condition are not well defined. On the other hand, the extrapolation scheme approximates the density and velocity at a solid boundary by a second-order polynomial; the unknown particle distribution function f is approximated by its equilibrium counterpart. Therefore, there is a need to develop an algorithm for the finite difference LBM that enables convenient application of boundary conditions similar to those specified for the numerical solution of the NS equations.

From the brief discussion on BGK/BE, it is clear that the objective of the present paper is to attempt to develop an alternative finite difference LBM based on the BGK/BE that can be used to simulate thermal fluid flows with correct γ and Pr in the subsonic to supersonic range, and where the numerical simulations can be performed stably. In addition, the boundary conditions at any open boundary and at the wall can be set as conveniently as those specified for the finite difference solution of the NS equations. Therefore, an alternative finite difference LBM to those discussed in [5,6] is sought, with the reference flow Reynolds number Re, γ, and Pr set a priori rather than as resolved parameters of the modeled BE. This requires an alternative f^{eq}. In the present approach, the shear stresses and the heat fluxes are determined as parameters in the constraints for finding the moments of f^{eq}; hence, they appear as additional terms in f^{eq}. A rigorous approach to address the setting of boundary conditions for f is proposed. It involves the development of an algorithm based on the use of a splitting technique for the alternative finite difference LBM that allows the boundary conditions to be set as conveniently as any finite difference methods for the solution of the NS equations.

II. Compressible Navier–Stokes Equations

The basis of the present analysis is the acoustics scaling form of the dimensionless NS equations. According to Lele [30], they can be written as

$$\frac{\partial \rho}{\partial t} + \frac{\partial \rho u_i}{\partial x_i} = 0 \tag{1}$$

$$\frac{\partial \rho u_i}{\partial t} + \frac{\partial \rho u_i u_j}{\partial x_j} = -\frac{\partial p}{\partial x_i} - \frac{\partial \tau_{ij}}{\partial x_j} \tag{2}$$

$$\frac{\partial \rho e_t}{\partial t} + \frac{\partial \rho u_i e_t}{\partial x_i} = -\frac{\partial p u_i}{\partial x_i} - \frac{\partial \tau_{ij} u_i}{\partial x_j} - \frac{\partial q_i}{\partial x_i} \tag{3}$$

where the equation of state $p = \rho e(\gamma - 1)$ has been invoked, the total energy e_t is defined as $e_t = e + (1/2)|\boldsymbol{u}|^2$, the viscous stress tensor τ_{ij} and the heat flux vector q_i are given by

$$\tau_{ij} = -\frac{M_\infty}{Re_\infty}\left\{2\mu\left(S_{ij} - \frac{1}{3}\delta_{ij}S_{kk}\right)\right\}$$
$$\text{with } S_{ij} \text{ defined by } S_{ij} = \frac{1}{2}\left(\frac{\partial u_i}{\partial x_j} + \frac{\partial u_j}{\partial x_i}\right) \tag{4}$$

$$q_i = -\frac{\gamma M_\infty}{Re_\infty Pr_\infty}\left(\kappa \frac{\partial e}{\partial x_i}\right) \tag{5}$$

Here, t is time, x_i is the position vector, u_i is the velocity vector, p is pressure, ρ is density, and e is the internal energy of the fluid. These symbols are used to denote dimensionless variables, whereas their dimensional counterparts are designated by the same symbols with a hat. The equations are derived using the characteristic scaling $\hat{L}$ for length, $\hat{c}_\infty$ for velocity, $\hat{L}/\hat{c}_\infty$ for time, $\hat{\rho}_\infty$ for density, $\hat{\rho}_\infty \hat{c}_\infty^2$ for pressure, $\hat{c}_\infty^2$ for energy, $\hat{\mu}_\infty$ for viscosity, and $\hat{\kappa}_\infty$ for conductivity. Therefore, $M_\infty = \hat{U}_\infty/\hat{c}_\infty$, $Re_\infty = \hat{\rho}_\infty \hat{L}\hat{U}_\infty/\hat{\mu}_\infty$, $Pr_\infty = \hat{\mu}_\infty(\hat{c}_p)_\infty/\hat{\kappa}_\infty$, $\mu = \hat{\mu}/\hat{\mu}_\infty$, $\kappa = \hat{\kappa}/\hat{\kappa}_\infty$, and $\hat{U}_\infty$ is the mean flow velocity. Here, the subscript ∞ is used to denote reference conditions. In these equations bold face and indices are used interchangeably to denote a vector, only indices are used to denote second-order tensors, and repeated indices are used to indicate summation over the order of the tensor. The local values of μ and κ can vary with space and time according to physical laws to be specified for the fluid under consideration.

III. Modeled Lattice Boltzmann Equation with $\gamma = 1.4$

The aim of the present study is to attempt a recovery of Eqs. (1–3) from the lattice counterpart of the BGK/BE with an alternative $\hat{f}^{\text{eq}}$ and a first-order Chapman–Enskog expansion of $\hat{f}$. Because an alternative finite difference LBM is chosen as the numerical scheme to solve the BGK/BE, it is appropriate to introduce the velocity space discretized form of this equation here. Only 1-D and 2-D flows are considered in the present paper, and therefore, the lattice equation in a 2-D domain is given. The 3-D counterpart can be easily obtained by following the same procedure. The velocity space discretized form of the BGK/BE is given by

$$\frac{\partial f_\alpha}{\partial t} + \boldsymbol{\xi}_\alpha \cdot \nabla_x f_\alpha = -\frac{1}{\tau Kn}(f_\alpha - f_\alpha^{\text{eq}}) \tag{6}$$

where α is the index of the lattice velocity and $\nabla_x = \partial/\partial x_i$. Again, acoustics scaling has been used to normalize Eq. (6), where the dimensionless quantities such as collision relaxation time τ, the particle velocity vector $\boldsymbol{\xi}_\alpha$, f_α, and f_α^{eq} are defined as $\tau = \hat{\tau}/\hat{\tau}_o$, $\boldsymbol{\xi}_\alpha = \hat{\boldsymbol{\xi}}_\alpha/\hat{c}_\infty$, and $(f_\alpha, f_\alpha^{\text{eq}}) = (\hat{f}_\alpha, \hat{f}_\alpha^{\text{eq}})/(\hat{\rho}_\infty/\hat{c}_\infty^D)$, respectively. $Kn = \hat{x}_o/\hat{L}$, $\hat{x}_o$ is the mesoscopic length scale, $\hat{\tau}_o = \hat{L}Kn/\hat{c}_\infty$ is the mesoscopic time scale, and $D = 2$ or 3 for 2-D or 3-D flows. It is assumed that $\hat{x}_o \ll \hat{L}$, and therefore, $\tau Kn \ll 1$. The macroscopic variables ρ, u_i, and e_t are given by [19]

$$\rho = \sum_{\alpha=0}^{N} f_\alpha \tag{7a}$$

$$\rho u_i = \sum_{\alpha=0}^{N} f_\alpha (\xi_\alpha)_i \tag{7b}$$

$$\frac{4}{D_T + D_R}(\rho e_t) = \sum_{\alpha=0}^{N} f_\alpha (\xi_\alpha)_i^2 \tag{7c}$$

Here, D_T and D_R are the translational and rotational degrees of freedom of the particles, respectively, and $\gamma = (D_T + D_R + 2)/(D_T + D_R)$ is obtained. For a diatomic gas, $D_T = 3$, $D_R = 2$, and thus $\gamma = 1.4$.

A D2Q9 lattice model was found to be sufficiently accurate for all problems attempted [20,21]. Therefore, only the derivation of a D2Q9 lattice f_α^{eq} is given here. For other flow types, a higher-order lattice model might be required; the corresponding f_α^{eq} can be similarly derived by following the present procedure. For a D2Q9 model, the lattice velocity is given by

$$\xi_0 = 0, \qquad \alpha = 0 \tag{8a}$$

$$\xi_\alpha = \sigma\{\cos[\pi(\alpha-1)/4], \sin[\pi(\alpha-1)/4]\}, \qquad \alpha = 1,3,5,7 \tag{8b}$$

$$\xi_\alpha = \sqrt{2}\sigma\{\cos[\pi(\alpha-1)/4], \sin[\pi(\alpha-1)/4]\}, \qquad \alpha = 2,4,6,8 \tag{8c}$$

where σ is a parameter to be determined. Just as in the case of the inviscid approach [20], a polynomial series in $(\xi_\alpha)_i$ up to second order is postulated for the discretized form of f_α^{eq}, i.e.,

$$f_\alpha^{\mathrm{eq}} = A_\alpha + (\xi_\alpha)_x Ax_\alpha + (\xi_\alpha)_y Ay_\alpha + (\xi_\alpha)_x^2 Bxx_\alpha + (\xi_\alpha)_y^2 Byy_\alpha + (\xi_\alpha)_x(\xi_\alpha)_y Bxy_\alpha \tag{9}$$

Here, the indices x and y are used to denote the stream and cross-stream direction in a 2-D flow and A_α, Ax_α, Bxx_α, and so forth are coefficients to be determined. This lattice f_α^{eq} is different from conventional ones, which are an expansion of the Maxwellian distribution function in terms of the products of u_i and $(\xi_\alpha)_i$ up to second [11] or third [15,22,25,] order. The present approach proposes a polynomial in terms of $(\xi_\alpha)_i$ and leaves the inclusion of u_i in the A_α, Ax_α, Bxx_α, etc., coefficients. Equation (9) is not an expansion in terms of u_i. Later derivation shows that u_i will appear in the coefficients of Eq. (9); however, it is not limited by the $M \ll 1$ assumption. Even then, the resulting f_α^{eq} can be recast into a form similar to conventional ones [11,22]. Thus determined, the Maxwellian distribution and the original BGK model can be recovered from Eq. (9) for the case of an inviscid incompressible flow of a monatomic gas [19,20].

The next step is to demonstrate that Eq. (9) is equivalent to Eqs. (1–3) with a D2Q9 lattice model by adopting a Chapman–Enskog expansion for f_α. The derivation is carried out by following the procedure outlined below. First, it is assumed that for each α, f_α can be expanded in terms of Kn to give

$$f_\alpha = f_\alpha^{(0)} + Kn f_\alpha^{(1)} + Kn^2 f_\alpha^{(2)} + \mathcal{O}(Kn^3) \tag{10}$$

The equations governing $f_\alpha^{(0)}$, $f_\alpha^{(1)}$, and $f_\alpha^{(2)}$ are obtained by substituting Eq. (10) into Eq. (6) and then collecting terms with the same order of Kn. The results are

$$f_\alpha^{(0)} = f_\alpha^{\mathrm{eq}}, \qquad \text{to } \mathcal{O}(Kn^0) \tag{11}$$

$$\frac{\partial f_\alpha^{(0)}}{\partial t} + (\xi_\alpha)_i \frac{\partial f_\alpha^{(0)}}{\partial x_i} = -\frac{f_\alpha^{(1)}}{\tau}, \qquad \text{to } \mathcal{O}(Kn^1) \tag{12}$$

$$\frac{\partial f_\alpha^{(1)}}{\partial t} + (\xi_\alpha)_i \frac{\partial f_\alpha^{(1)}}{\partial x_i} = -\frac{f_\alpha^{(2)}}{\tau}, \qquad \text{to } \mathcal{O}(Kn^2) \tag{13}$$

In the conventional approach, Eq. (12) is used to establish equivalency with the Euler equation, while Eqs. (12) and (13) are used to recover the NS equations. The present approach adopts the view point that equivalency with the NS equations could be established with Eq. (12) under certain constraints to be stipulated on f_α^{eq}. These constraints consist of the macroscopic properties given in Eqs. (7a–7c) plus others derived making use of Eqs. (2) and (3). For 2-D flows ($D = 2$), the results (with $N = 8$) are

$$\sum_{\alpha=0}^{N} f_\alpha^{\mathrm{eq}} = \rho \tag{14a}$$

$$\sum_{\alpha=0}^{N} f_\alpha^{\mathrm{eq}} (\xi_\alpha)_x = \rho u \tag{14b}$$

$$\sum_{\alpha=0}^{N} f_\alpha^{\mathrm{eq}} (\xi_\alpha)_y = \rho v \tag{14c}$$

$$\sum_{\alpha=0}^{N} f_\alpha^{\mathrm{eq}} \{(\xi_\alpha)_x^2 + (\xi_\alpha)_y^2\} = \frac{4}{D_T + D_R}(\rho e_t) \tag{14d}$$

$$\sum_{\alpha=0}^{N} f_\alpha^{\mathrm{eq}} (\xi_\alpha)_x^2 = \rho u^2 + p + \tau_{xx} + P'_{xx} \tag{15a}$$

$$\sum_{\alpha=0}^{N} f_\alpha^{\mathrm{eq}} (\xi_\alpha)_y^2 = \rho v^2 + p + \tau_{yy} + P'_{yy} \tag{15b}$$

$$\sum_{\alpha=0}^{N} f_\alpha^{\mathrm{eq}} (\xi_\alpha)_x (\xi_\alpha)_y = \rho uv + \tau_{xy} + P'_{xy} \tag{15c}$$

$$\sum_{\alpha=0}^{N} f_\alpha^{\mathrm{eq}} \{(\xi_\alpha)_x^2 + (\xi_\alpha)_y^2\}(\xi_\alpha)_x = \frac{4}{D_T + D_R}[u(p + \rho e_t) + u\tau_{xx} + v\tau_{xy} + q_x] \tag{16a}$$

$$\sum_{\alpha=0}^{N} f_\alpha^{\mathrm{eq}} \{(\xi_\alpha)_x^2 + (\xi_\alpha)_y^2\}(\xi_\alpha)_y = \frac{4}{D_T + D_R}[v(p + \rho e_t) + u\tau_{xy} + v\tau_{yy} + q_y] \tag{16b}$$

where P'_{xx}, P'_{yy}, P'_{xy} are elements of a second-order tensor P'_{ij} in 2-D flows. The first group of constraints [Eqs. (14a–14d)] are the 2-D equivalent of Eqs. (7a–7c), the second group [Eqs. (15a–15c)] are constraints derived by requiring Eq. (2) to be satisfied identically, while the third group [Eqs. (16a) and (16b)] are similarly obtained by requiring the satisfaction of Eq. (3). The specification of these latter two groups of constraints ensures that Eq. (6) is equivalent to the NS equations correct to order Kn. In addition, higher-order moments of f_α^{eq} are assumed to vanish, i.e.,

$$\sum_{\alpha=0}^{N} f_\alpha^{(n)} = 0 \quad \text{for } n \geq 1 \tag{17a}$$

$$\sum_{\alpha=0}^{N} f_\alpha^{(n)} (\xi_\alpha)_x = 0 \quad \text{for } n \geq 1 \tag{17b}$$

$$\sum_{\alpha=0}^{N} f_\alpha^{(n)} (\xi_\alpha)_y = 0 \quad \text{for } n \geq 1 \tag{17c}$$

$$\frac{D_T + D_R}{4} \sum_{\alpha=0}^{N} f_\alpha^{(n)} \{(\xi_\alpha)_x^2 + (\xi_\alpha)_y^2\} = 0 \quad \text{for } n \geq 1 \tag{17d}$$

Secondly, multiplying Eq. (6) with respect to $\{1, (\xi_\alpha)_i, (|(\xi_\alpha)_i|^2)(D_T + D_R)/4\}^T$ and taking summation over α, then substituting Eq. (10) into these resulting equations and making use of the constraints given in Eqs. (14a–14d) and (17a–17d), the final macrotransport equations for a 2-D flow in Cartesian coordinates are obtained

$$\frac{\partial \rho}{\partial t} + \frac{\partial \rho u}{\partial x} + \frac{\partial \rho v}{\partial y} + \mathcal{O}(Kn) = 0 \tag{18a}$$

$$\frac{\partial (\rho u)}{\partial t} + \frac{\partial}{\partial x}(\rho u^2 + p + \tau_{xx} + P'_{xx}) + \frac{\partial}{\partial y}(\rho uv + \tau_{xy} + P'_{xy}) + \mathcal{O}(Kn) = 0 \tag{18b}$$

$$\frac{\partial (\rho v)}{\partial t} + \frac{\partial}{\partial x}(\rho uv + \tau_{xy} + P'_{xy}) + \frac{\partial}{\partial y}(\rho v^2 + p + \tau_{yy} + P'_{yy}) + \mathcal{O}(Kn) = 0 \tag{18c}$$

$$\frac{\partial}{\partial t}(\rho e_t) + \frac{\partial}{\partial x}[u(\rho e_t + p) + u\tau_{xx} + v\tau_{xy} + q_x] + \frac{\partial}{\partial y}[v(\rho e_t + p) + u\tau_{xy} + v\tau_{yy} + q_y] + \mathcal{O}(Kn) = 0 \tag{18d}$$

where $p = \rho e(\gamma - 1)$ has been assumed and $\gamma = 1.4$ follows from $\gamma = (D_T + D_R + 2)/(D_T + D_R)$. If the full set of NS equations for

2-D flows were to be recovered correct to order Kn, the elements of P'_{ij} have to satisfy the divergence condition, that is

$$\frac{\partial P'_{ij}}{\partial x_j} = 0 \tag{19}$$

This implies that the present approach requires the simultaneous solution of Eqs. (6) and (19). Solution of Eq. (19) for 2-D flows is detailed in Sec. IV, and that of Eq. (6) is detailed in Sec. V.

Third, the coefficients of Eq. (9) can now be determined. Of the nine equations given by Eqs. (14a–14d), (16a), and (16b), only eight are independent because one is a duplicate of the kinetic energy equation. These equations are used to evaluate A_α, Ax_α, Bxx_α, etc. If the coefficients having the same energy shell of the lattice velocities are assumed to be the same, the number of unknowns resulting from the coefficients A_α, Ax_α, Bxx_α, etc. are 13 in a D2Q9 lattice model. Because the number of constraints available for the determination of these coefficients is 8 there is certain flexibility, and assumptions can be made to facilitate solutions of the equations. As a first attempt, 5 coefficients out of the 13 are assumed zero; these 5 coefficients are A_1, A_2, Bxx_2, Byy_2, and Bxy_1. Details of this derivation are given in Fu et al. [20]. The results are:

$$A_0 = \rho - \frac{2p}{\sigma^2} - (\gamma-1)\frac{\rho|\boldsymbol{u}|^2}{\sigma^2}, \qquad A_1 = A_2 = 0 \tag{20a}$$

$$Ax_1 = \frac{\rho u}{\sigma^2} - \frac{\gamma p u}{\sigma^4} - (\gamma-1)\frac{1}{2}\frac{\rho|\boldsymbol{u}|^2 u}{\sigma^4} - (\gamma-1)\frac{q_x + u\tau_{xx} + v\tau_{xy}}{\sigma^4} \tag{20b}$$

$$Ax_2 = -\frac{1}{4}\frac{\rho u}{\sigma^2} + \frac{1}{2}\frac{\gamma p u}{\sigma^4} + (\gamma-1)\frac{1}{4}\frac{\rho|\boldsymbol{u}|^2 u}{\sigma^4} + (\gamma-1)\frac{q_x + u\tau_{xx} + v\tau_{xy}}{2\sigma^4} \tag{20c}$$

$$Ay_1 = \frac{\rho v}{\sigma^2} - \frac{\gamma p v}{\sigma^4} - (\gamma-1)\frac{1}{2}\frac{\rho|\boldsymbol{u}|^2 v}{\sigma^4} - (\gamma-1)\frac{q_y + u\tau_{xy} + v\tau_{yy}}{\sigma^4} \tag{20d}$$

$$Ay_2 = -\frac{1}{4}\frac{\rho v}{\sigma^2} + \frac{1}{2}\frac{\gamma p v}{\sigma^4} + (\gamma-1)\frac{1}{4}\frac{\rho|\boldsymbol{u}|^2 v}{\sigma^4} + (\gamma-1)\frac{q_y + u\tau_{xy} + v\tau_{yy}}{2\sigma^4} \tag{20e}$$

$$Bxx_1 = \frac{1}{2\sigma^4}(p + \rho u^2 + \tau_{xx} + P'_{xx}), \qquad Bxx_2 = 0 \tag{20f}$$

$$Byy_1 = \frac{1}{2\sigma^4}(p + \rho v^2 + \tau_{yy} + P'_{yy}), \qquad Byy_2 = 0 \tag{20g}$$

$$Bxy_2 = \frac{1}{4\sigma^4}(\rho uv + \tau_{xy} + P'_{xy}), \qquad Bxy_1 = 0 \tag{20h}$$

It should be emphasized that the set of coefficients deduced for a D2Q9 model is not unique; other choices besides setting the 5 coefficients to zero could be made. However, all choices should be dictated by the necessity to recover a f_α^{eq} similar to those given in [11,15,22,25,] obtained by expanding the Maxwellian distribution. In the present approach, recasting Eq. (9) to a form similar to previous f_α^{eq} can be easily carried out and the result is

$$\begin{aligned} f_\alpha^{\mathrm{eq}} = {} & C_\alpha + C_{0\alpha}|\boldsymbol{u}|^2 + (\xi_\alpha)_x C_{1\alpha x} + (\xi_\alpha)_y C_{1\alpha y} + (\xi_\alpha)_x u C_{2\alpha xx} \\ & + (\xi_\alpha)_x v C_{2\alpha xy} + (\xi_\alpha)_y u C_{2\alpha yx} + (\xi_\alpha)_y v C_{2\alpha yy} \\ & + (\xi_\alpha)_x|\boldsymbol{u}|^2 u C_{3\alpha xx} + (\xi_\alpha)_x|\boldsymbol{u}|^2 v C_{3\alpha xy} + (\xi_\alpha)_x^2 C_{4\alpha xx} \\ & + (\xi_\alpha)_y^2 C_{4\alpha yy} + (\xi_\alpha)_x(\xi_\alpha)_y C_{4\alpha xy} + (\xi_\alpha)_x^2 u^2 C_{5\alpha xx} \\ & + (\xi_\alpha)_y^2 v^2 C_{5\alpha yy} + (\xi_\alpha)_x(\xi_\alpha)_y uv C_{5\alpha xy} \end{aligned} \tag{21}$$

This form only has terms up to the second order of $(\xi_\alpha)_i$, u_i, and their products; it is different from Watari's [22] expression in two ways. First, it does not include third-order terms in $(\xi_\alpha)_i$, u_i, and their products; second, it also has terms such as $(\xi_\alpha)_x C_{1\alpha x}$, $(\xi_\alpha)_y C_{1\alpha y}$, $(\xi_\alpha)_x^2 C_{4\alpha xx}$, $(\xi_\alpha)_y^2 C_{4\alpha yy}$, and $(\xi_\alpha)_x(\xi_\alpha)_y C_{4\alpha xy}$. It seems that Eq. (9) together with coefficients given in Eqs. (20a–20h) constitutes an alternative method to deduce a f_α^{eq} that is not limited by $M \ll 1$.

It is noted that there are no undefined constants except σ, which is bounded by the relation deduced from Eq. (14d) and can be written as

$$\begin{aligned} \min(|\xi_\alpha|^2)\sum_{\alpha=0}^{N} f_\alpha^{\mathrm{eq}} &\le \frac{4}{D_T + D_R}\left(\rho e + \frac{1}{2}\rho|\boldsymbol{u}|^2\right) \\ &\le \max(|\xi_\alpha|^2)\sum_{\alpha=0}^{N} f_\alpha^{\mathrm{eq}} \end{aligned} \tag{22}$$

As a result, there are no arbitrary constants in the entire formulation. It will be shown in the validation simulations presented below that the setting of τ is not crucial; it only has to satisfy the condition that $\tau Kn \ll 1$.

IV. Solution of P'_{ij}

The individual elements of P'_{ij} are obtained by solving Eq. (19) and the relation $\sum P'_{kk} = A$ where $A = [\{D - (D_T + D_R)/(D_T + D_R)\}]\rho|\boldsymbol{u}|^2 - \sum \tau_{kk}$ for viscous formulation, while the viscous stress term τ_{kk} in A is identically zero for the inviscid approach [20]. All the macroscopic quantities (ρ, u_i, p), including the physical boundary, are contained in A. In the 2-D case considered here, these equations reduce to

$$\frac{\partial P'_{xx}}{\partial x} + \frac{\partial P'_{xy}}{\partial y} = 0 \tag{23a}$$

$$\frac{\partial P'_{xy}}{\partial x} + \frac{\partial P'_{yy}}{\partial y} = 0 \tag{23b}$$

$$P'_{xx} + P'_{yy} = A \tag{23c}$$

For the present analysis it is assumed that all functions are sufficiently smooth for their derivatives to exist. A Poisson equation can be derived from Eqs. (23a–23c) through differentiation; the result is

$$\frac{\partial^2 A}{\partial x \partial y} + \left(\frac{\partial^2}{\partial x^2} + \frac{\partial^2}{\partial y^2}\right)P'_{xy} = 0 \tag{24}$$

On the other hand, taking the derivative of Eq. (23a) with respect to x, that of Eq. (23b) with respect to y, and then subtracting, the following is obtained:

$$\frac{\partial^2 P'_{xx}}{\partial x^2} - \frac{\partial^2 P'_{yy}}{\partial y^2} = 0 \tag{25}$$

After using Eq. (23c), another Poisson equation is obtained, that is

$$-\frac{\partial^2 A}{\partial y^2} + \left(\frac{\partial^2}{\partial x^2} + \frac{\partial^2}{\partial y^2}\right)P'_{xx} = 0 \tag{26}$$

Similarly, an equation for P'_{yy} can be deduced. Solving Eqs. (24) and (26) with suitable boundary conditions and using Eq. (23c),

P'_{xy}, P'_{xx}, and P'_{yy} can be determined. The boundary conditions for these equations are given below.

A finite rectangular computational domain with four boundaries, namely top, bottom, left, and right, represented by $y = H$, $y = 0$, $x = 0$, and $x = L$, respectively, is assumed. In solving Eq. (24), the Neumann condition is assumed for the top and bottom boundaries, that is

$$\frac{\partial P'_{xy}}{\partial y} = 0 \quad \text{at } y = 0, H \tag{27}$$

while the Dirichlet condition is assumed for the left and right boundaries, or

$$P'_{xy} = k_{1L} \quad \text{at } x = 0, \qquad P'_{xy} = k_{1R} \quad \text{at } x = H \tag{28}$$

where k_{1L} and k_{1R} are constants. On the other hand, in solving Eq. (26), the Dirichlet condition is invoked for the top and bottom boundaries

$$P'_{xx} = k_{2B} \quad \text{at } y = 0, \qquad P'_{xx} = k_{2T} \quad \text{at } y = H \tag{29}$$

where k_{2B} and k_{2T} are constants, and the Neumann condition is prescribed for the left and right boundaries, or

$$\frac{\partial P'_{xx}}{\partial x} = 0 \quad \text{at } x = 0, L \tag{30}$$

Details of the determination of k_{1L}, k_{1R}, and so forth are given in Appendix A.

V. Finite Difference Lattice Boltzmann Method and its Numerical Simulation

Equation (6) is a system of inhomogeneous hyperbolic equations; thus, any standard finite difference scheme can be used to solve it. Conventional LBM is only second-order accurate in both spatial and temporal dimensions; thus, it is not sufficiently accurate for aeroacoustics simulations. In recent investigations, including the solution technique proposed in [19], the term on the right hand side (RHS) of Eq. (6) is evaluated locally at every time step. A second-order Runge–Kutta time marching scheme is used to calculate the time-dependent term in Eq. (6), while the second term on the left hand side (LHS) of Eq. (6) is estimated using a sixth-order compact finite difference scheme [30,31]. This numerical scheme is accurate enough to allow the aeroacoustic disturbances to be resolved correctly [19,20]. Further, it is different from the conventional LBM because it requires the complete equation including the RHS of Eq. (6) to be discretized and solved simultaneously, and is sixth-order accurate. This alternative finite difference LBM scheme is simply designated as FDLBM to distinguish it from the conventional LBM and from the finite difference LBM proposed in [5,6].

Because the boundary value of f_α has to be specified at every time step, this renders the solution procedure slightly more complicated. It is no easy task to set a proper boundary condition for f_α because for any physical boundary condition stipulated for macroscopic quantities, it is sometimes difficult to find a corresponding f_α, and the traditional bounceback wall boundary condition is not quite suitable. To specify the boundary conditions for the modeled BE as freely as any conventional finite difference scheme for the solution of the NS equations, it is proposed to solve Eq. (6) using a splitting technique, which is a common approach for solving partial differential equations with source terms [32]. Therefore, Eq. (6) is solved in three steps: an initialization step, a freestreaming step, and a collision step.

In the initialization step, the initial conditions of all macroscopic quantities are specified to allow the streaming step to march ahead. For the freestreaming step, the homogenous hyperbolic equation is solved

$$\frac{\partial f_\alpha}{\partial t} + \boldsymbol{\xi}_\alpha \cdot \nabla_x f_\alpha = 0 \tag{31}$$

Then, the results obtained in this streaming step provide the necessary initial conditions for the equation governing the collision step

$$\frac{\partial f_\alpha}{\partial t} = -\frac{1}{\tau Kn}(f_\alpha - f_\alpha^{\mathrm{eq}}) \tag{32a}$$

The Euler method with the choice $\Delta t = \tau Kn$ is used to discretize Eq. (32a), thus giving

$$\frac{f_\alpha(\mathbf{x}, t + \Delta t) - f_\alpha(\mathbf{x}, t)}{\Delta t} = -\frac{1}{\tau Kn}(f_\alpha(\mathbf{x}, t) - f_\alpha^{\mathrm{eq}}(\mathbf{x}, t))$$
$$\Rightarrow f_\alpha(\mathbf{x}, t + \Delta t) = f_\alpha^{\mathrm{eq}}(\mathbf{x}, t) \tag{32b}$$

The procedure for each step is briefly described below.

Initialization step:

1) Initial conditions for all macroscopic quantities (u_0, v_0, p_0, ρ_0) including the boundary points are given.

2) The initial equilibrium distribution function $f_\alpha^{0,\mathrm{eq}}$ (including the boundary points) is determined using Eq. (9). These are used as initial values to start the solution of Eq. (6). In this setting, it is assumed that the initial distribution function is "relaxed" to its equilibrium state under the BGK model.

Freestreaming step:

1) With the distribution function f_α at time t (including the boundary points) known, a second-order Runge–Kutta time marching scheme is invoked for the time-dependent term in Eq. (31), and a compact sixth-order finite difference scheme is used to handle the second term in Eq. (31) spatially. This is only applied to the interior grid points in the domain. The result gives the intermediate value f_α^I (excluding boundary points).

2) Using this f_α^I and Eqs. (7a–7c), the corresponding macroscopic quantities (ρ_I, u_I, v_I, p_I) for all interior grid points are calculated.

3) The boundary conditions for the macroscopic level are then set (e.g., $u_I = v_I = 0$ for no-slip wall boundary).

4) Using the macroscopic quantities thus determined (complete domain including the boundary points) and invoking Eq. (9), a corresponding $f_\alpha^{I,\mathrm{eq}}$ is obtained (including all boundary points). This $f_\alpha^{I,\mathrm{eq}}$ can be different from f_α^I in (step 2 of the freestreaming step).

Collision step:

1) Because of Eq. (32b), the collision step is completed by exactly setting the new f_α (at time $t + \Delta t$) as the equilibrium distribution function $f_\alpha^{I,\mathrm{eq}}$. Because each set of macroscopic quantities will map uniquely to an equilibrium distribution function, and vice versa, the macroscopic quantities thus obtained are the values at time $t + \Delta t$, that is, $(\rho, u, v, p)|_{t+\Delta t} = (\rho_I, u_I, v_I, p_I)$.

2) Time marching proceeds by repeating procedures 2–3 of the freestreaming step).

The relaxation time τ in Eq. (6) can be specified as follows. In the present formulation, τ and Kn always appear as τKn, implying that τ and Kn need not be specified separately. Because τ is of $\mathcal{O}(1)$ and Kn is assumed to be very small, of the order of 10^{-7} according to [2], the term τKn should be much smaller than 1 when compared with other terms in Eq. (6). In the present calculation, the choice of $\Delta t = \tau Kn = 10^{-5}$ is sufficient to give results identical to those obtained from direct numerical simulation (DNS); also, numerical instability was not encountered even without using high-order filters.

An absorbing boundary condition using a unit dimensionless absorbing region gives reliable and accurate results compared with those obtained from DNS simulations [33]; therefore, it is adopted in the present study. The damping coefficient as defined in [33] is $\sigma_d = \sigma_m(\delta/D_d)^2$ where σ_m is a constant to be specified, δ is the distance measured from the start of the damping region, and D_d is its width. The choice of σ_m varies from problem to problem and, quite often, σ_m is determined by trial and error for each problem. In the present study a D2Q9 model is used, similar to all calculations carried out in [19,33,34]. On open boundaries, a one-sided fourth-order compact method is used to derive the first derivatives. This is essentially a low-dispersive and low-dissipative scheme and is most suitable for simulation of aeroacoustics problems [31,35,36]. The P'_{ij} boundary conditions have already been discussed in Sec. IV.

VI. Validation of Finite Difference Lattice Boltzmann Method Against Benchmark Problems

The FDLBM is examined for its validity and extent against three different types of compressible flows: thermal Couette flow, aeroacoustics, and shock structure problems. The thermal Couette flow admits to an analytical solution and has been treated previously [22,23]. In aeroacoustics problems, sample cases are selected to test the effectiveness of the proposed no-slip boundary conditions, the ability of the BGK/BE plus the proposed f_α^{eq} to reproduce the effect of Re, and the ability to replicate vorticity-acoustics and entropy-acoustics interactions correctly. The shock structure problems are selected to show that the FDLBM can be generalized to treat complicated thermodynamic models, such as the Brenner–NS model [37,38]. They are not selected to test the upper Mach number limit of the FDLBM.

Wherever possible, the FDLBM simulations are either validated against analytical solutions or against DNS results obtained by solving the NS equations using an explicit fourth-order Runge–Kutta time marching scheme for the time-dependent term in Eqs. (1–3), and the five-point sixth-order compact finite difference scheme of Lele [30] for the spatial derivatives. High-order filtering of Visbal and Gaitonde [39] is applied in every final stage of the Runge–Kutta scheme to suppress numerical instabilities due to spatial differencing. This numerical scheme is known to give very accurate DNS results for aeroacoustics problems [40]. No-slip boundary conditions are invoked at solid boundaries, while the absorbing boundary condition used in [33,40] is adopted for all computational boundaries other than solid walls. For steady-state problems, the calculation is considered steady when the convergence criterion $\max \|\partial Q\| \le \varepsilon$ is satisfied. Here, Q represents all macroscopic quantities (ρ, u, v, p) and the operator ∂ signifies the difference between two successive time steps, and $\varepsilon = 10^{-6}$ is specified. Finally, for the sake of clarity, numerical details for each individual case are specified separately in the following sections.

Unless otherwise specified, σ is estimated from Eq. (22) for all cases investigated using the present approach. In this paper, it is chosen as

$$\sigma = \sqrt{(1/N)\sum\{4/(D_T + D_R)\}\{\rho e + \rho|\boldsymbol{u}|^2/2\}}$$

where N is the total number of points in the computational domain. All other constants are either derived analytically or known; therefore, no arbitrary constants are required. This is a distinct advantage of the FDLBM compared with conventional LBM and other finite difference LBMs. The error norms between the FDLBM and analytical or DNS of the NS equations of a macroscopic variable $\boldsymbol{b}$ are expressed in terms of the L_q integral norm for any integer q. This L_q integral norm and its maximum are given by

$$\|L_q(\boldsymbol{b})\| = \left[\frac{1}{N}\sum_{j=1}^{N}|\boldsymbol{b}_{\text{LBM},j} - \boldsymbol{b}_{\text{DNS},j}|^q\right]^{\frac{1}{q}} \tag{33a}$$

$$\|L_\infty(\boldsymbol{b})\| = \max_j|\boldsymbol{b}_{\text{LBM},j} - \boldsymbol{b}_{\text{DNS},j}| \tag{33b}$$

A. Thermal Couette Flow

The dissipative characteristics of the BGK/BE can be verified by using it to simulate thermal Couette flows [22,23]. A thermal Couette flow is defined by an upper wall with internal energy e_2 moving at speed U that is H apart from a stationary lower wall with internal energy $e_1 \le e_2$. All parameters are normalized. The theoretical solution for e at steady state is given by

$$e = e_1 + (e_2 - e_1)\frac{y}{H} + \frac{\text{Pr}}{2\gamma}U^2\frac{y}{H}\left(1 - \frac{y}{H}\right) \tag{34}$$

The computational domain for this problem is given by $0 \le x, y \le 1$, with $H = 1$, $\Delta x = \Delta y = 0.02$, and $\Delta t = 10^{-4}$ chosen for the numerical simulation. In this case, there is no need to use a sixth-order numerical scheme; the Boltzmann equation is solved using a second-order central difference scheme for spatial derivatives and a second-order Runge–Kutta scheme for time marching. Periodic boundary conditions are applied on the left and right boundary and no-slip conditions are invoked on the walls. Two cases are attempted; case 1 with $e_2 = e_1$ and case 2 with $e_2 = 1.5e_1$. For both cases, $U = 1$, $\gamma = 1.4$, and $Pr = 0.84$ are assumed. The results are plotted in Fig. 1 for comparison. Excellent agreement is obtained between theory and FDLBM simulation, thus showing that the FDLBM with an alternative f_α^{eq} is appropriate for thermal flow simulations.

B. Aeroacoustics Problems

Direct aeroacoustics simulation (DAS) is taxing on the numerical scheme as well as on the modeled BE. The reason is the disparity of scales [19] and the numerical accuracy required if the aeroacoustics scales were to be resolved correctly [31]. If the FDLBM could replicate benchmark thermal and aeroacoustics problems correctly, including resolving the nonlinear interactions between flow and acoustics and the effect of Re on these interactions, then a claim on the validity and extent of the BGK/BE with the proposed f_α^{eq} can be made. A comparison of the L_q between the FDLBM and the results of [19] could demonstrate the appropriateness of the present f_α^{eq} versus the slightly modified conventional f_α^{eq}.

1. *Aeroacoustics Case 1: Circular Pulse in an Infinite Medium*

A circular pressure pulse located at $(x, y) = (0, 0)$ initially with distribution given by

$$\rho = \rho_\infty, \qquad u = 0, \qquad v = 0$$
$$p = p_\infty + \varepsilon\exp[-\ell n\, 2 \times \{(x^2 + y^2)/0.2^2\}] \tag{35}$$

is propagating in an infinite medium where $u_\infty = 0$, $\rho_\infty = 1$, $p_\infty = 1/\gamma$, and ε is chosen to be $\varepsilon = 1 \times 10^{-4}$. This pulse is simulated using FDLBM and DNS. Other numerical conditions specified are $\Delta t = 0.00001$, $\Delta x = \Delta y = 0.05$; computational domain is bounded by $-3.5 \le x(y) \le 3.5$ with one unit of buffer region (i.e., the actual domain is given by $-2.5 \le x(y) \le 2.5$), $Pr_\infty = 0.71$, and $Re_\infty = 10$, 100, 1000, and ∞. The numerical settings for DNS are given by $\Delta x = \Delta y = 0.05$, $\Delta t = 0.001$. Therefore, the ratios $\Delta x/\Delta t$ and $\Delta y/\Delta t$ for the FDLBM are 5×10^3 and are not related to sound speed c as previous work on conventional LBM suggested that they should. Further, these ratios do not have any effect on the FDLBM simulations. The error norms are compared in Table 1.

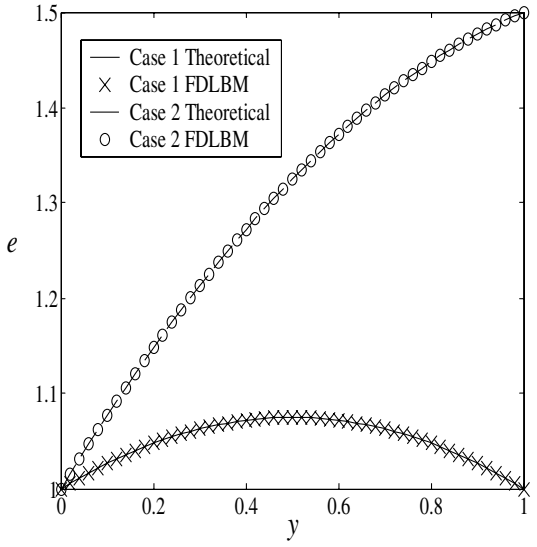

Fig. 1 Comparison of the theoretical and FDLBM results for two thermal Couette flow cases; case 1 has $e_2 = e_1$, and case 2 has $e_2 = 1.5e_1$.

Table 1 Error norms comparison between finite difference lattice Boltzmann method and direct numerical simulation results for different Re_∞ of aeroacoustics case: circular pulse in infinite medium

Error norms	L_∞	L_2	L_1
	$Re_\infty = 1000$		
p	8.7550e − 009	1.0654e − 009	4.9497e − 010
ρ	8.8638e − 009	1.0758e − 009	4.9729e − 010
u	6.3735e − 009	7.5287e − 010	3.2272e − 010
	$Re_\infty = 100$		
p	5.7035e − 009	1.1822e − 009	7.2596e − 010
ρ	6.1154e − 009	1.2057e − 009	7.3706e − 010
u	3.9890e − 009	9.6252e − 010	4.9804e − 010
	$Re_\infty = 10$		
p	3.1593e − 009	1.2003e − 009	1.0099e − 009
ρ	3.5221e − 009	1.2846e − 009	1.0728e − 009
u	2.8582e − 009	1.2332e − 009	9.9919e − 010

Only the results that clearly show the Re_∞ effect on the spread of the pulse are plotted in Fig. 2 for comparison; the distributions of p and ρ along the x axis at $t = 1$ are shown. The role of viscosity is to disperse the wave and this is clearly illustrated in the $Re_\infty = 100$ and 10 panels of Fig. 2. As Re_∞ decreases, the diffusion of the wave becomes more and more pronounced, thus reflecting in a substantial reduction of the peak amplitude. When Re_∞ increases to 1000 it is sufficiently inviscid because the solution is essentially identical to the inviscid result. Contour plots of $p - p_\infty$ and $u - u_\infty$ are similar to the inviscid case [20] and are essentially identical for the FDLBM and DNS simulations; the error norms tabulated in Table 1 lend evidence to this claim. The largest error norm is of the order of 10^{-9} and the smallest is of order 10^{-10}. This is true for all Re_∞ examined. These error norms represent at least two orders improvement for all Re_∞ investigated compared with those reported in [19], where a slightly modified expansion of the Maxwellian distribution for f_α^{eq} is used. This shows that the alternative f_α^{eq} proposed here is better suited for aeroacoustics simulations than the modified expansion obtained from the Maxwellian distribution.

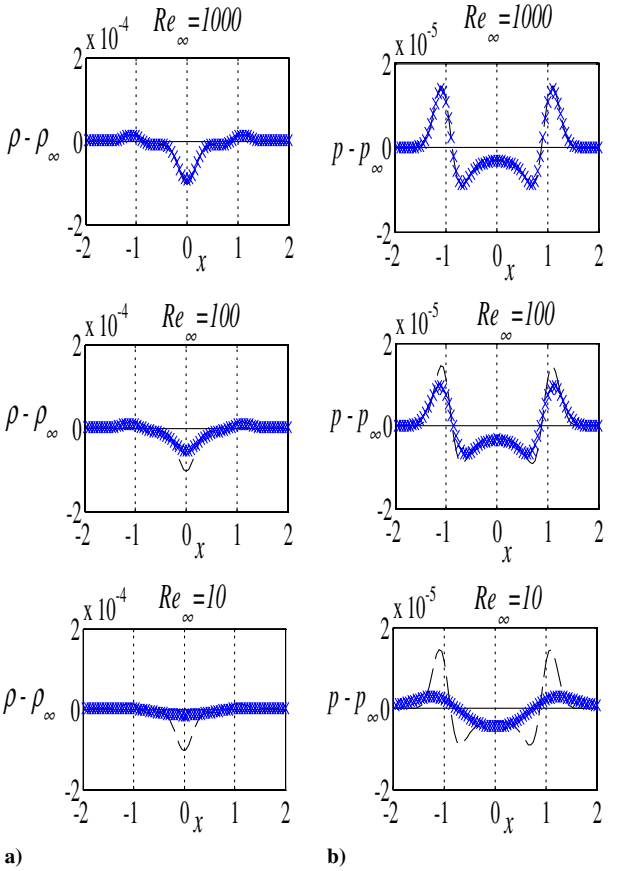

Fig. 2 Distribution of ρ and p at $t = 1$ for different Re_∞ along x axis: a) ρ, and b) p. The dashed curve is the inviscid solution, the continuous curve represents the DNS results, and the crosses represent the FDLBM result. In these plots, the DNS and FDLBM results essentially overlap each other.

2. *Aeroacoustics Case 2: Circular Pulse in an Enclosure*

To illustrate the effectiveness of the proposed wall boundary condition for f, the propagation of a pressure pulse inside an enclosure is investigated. The pulse is located at $(x, y) = (-1, 0)$ with initial conditions given by

$$\rho = \rho_\infty, \qquad u = u_\infty, \qquad v = v_\infty$$
$$p = p_\infty + \varepsilon \exp[-\ell_n 2 \times ((x+1)^2 + y^2)/0.2^2] \tag{36}$$

For this example, $u_\infty = v_\infty = 0$, $\rho_\infty = 1$, $p_\infty = 1/\gamma$, $\varepsilon = 10^{-4}$ are chosen together with $Re_\infty = 1000$, $Pr_\infty = 0.71$, and $\gamma = 1.4$. Again, the numerical settings are given by $\Delta x = \Delta y = 0.05$, while $\Delta t = 0.001$ is selected for DNS, and $\Delta t = 0.00001$ for FDLBM. The effectiveness of the proposed wall boundary condition for f can be best illustrated by plotting the contour maps of $p - p_\infty$ and $u - u_\infty$ at $t = 3$ and 6 in Fig. 3a. They show that there is no accumulation of reflected waves inside the enclosure. The FDLBM and DNS results are plotted in the upper and lower half of Fig. 3a, respectively. These contours display identical behavior. The importance of P'_{ij} to the entire simulation can be demonstrated by plotting P'_{xy} (at $t = 3$ and 6) in Fig. 3b. The contours display similar patterns to those shown for $p - p_\infty$ and $u - u_\infty$ in Fig. 3a. The error norms between the FDLBM and DNS results are tabulated in Table 2; the smallest error norm is of order 10^{-10} and the largest is of order 10^{-8}, consistent with case 1. Clearly, these results show that the wall boundary conditions proposed for f are valid.

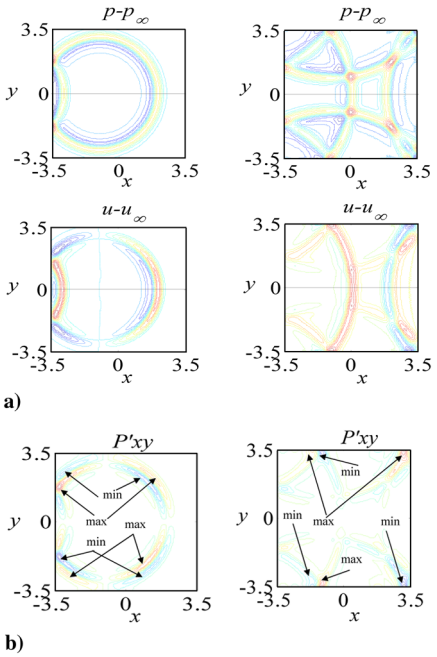

Fig. 3 Plots of: a) contour map of p and u fluctuation at $t = 3.0$ and $t = 6.0$. The lower half is the DNS solution, and the upper half is the FDLBM result. There are 16 equally distributed contour lines in each plot; the (max, min) values at $t = 3.0$ are 1.5164e − 005, −7.9352e − 006 for p, and 9.9756e − 006, −5.4574e − 006 for u. At $t = 6.0$ they are 9.9848e − 006, −5.0447e − 006 for p, and 6.6799e − 006, −8.9818e − 006 for u, respectively. The contours decrease from the maximum outward. Illustrations of: b) contour map of P'_{xy} fluctuation at $t = 3.0$ and $t = 6.0$. There are 16 equally distributed contour lines in each plot; the (max, min) values at $t = 3.0$ are 2.2863e − 008, −2.2922e − 008, and at $t = 6.0$ are 2.7008e − 008, −2.7036e − 008. The maximum and minimum contours are as indicated; in the case of maximum they decrease outward, and in the case of minimum they increase outward.

Table 2 Error norms comparison between finite difference lattice Boltzmann method and direct numerical simulation results with $Re_\infty = 1000$ for aeroacoustics case: circular pulse in an enclosure

Error norms	L_∞	L_2	L_1
	$t = 3$		
p	1.5845e − 008	2.1043e − 009	1.0799e − 009
ρ	1.6342e − 008	2.1771e − 009	1.1217e − 009
u	1.0815e − 008	1.4520e − 009	7.1250e − 010
	$t = 6$		
p	5.9506e − 008	3.9741e − 009	2.6555e − 009
ρ	7.4089e − 008	4.2248e − 009	2.7627e − 009
u	3.2291e − 008	2.6228e − 009	1.5861e − 009

3. *Aeroacoustics Case 3: Three Pulses in a Uniform Stream*

The three pulses are a pressure, a vorticity, and an entropy pulse propagating in a uniform mean flow u_∞. Only the pressure pulse is propagating with c; the entropy and the vortex pulse move with u_∞. The initial conditions are given by Tam and Webb [41] as

$$\rho = \rho_\infty + \varepsilon_1 e^a + \varepsilon_2 e^b, \qquad p = p_\infty + \varepsilon_1 e^a \tag{37a}$$

$$u = u_\infty + \varepsilon_2 y e^b, \qquad v = v_\infty - \varepsilon_2 (x-1) e^b \tag{37b}$$

$$\alpha = -\ln 2 \times [\{(x+1)^2\}/0.4^2]$$
$$b = -\ln 2 \times [\{(x-1)^2\}/0.4^2] \tag{37c}$$

where $\rho_\infty = 1$, $u_\infty = 0.9$, $v_\infty = 0$, $p_\infty = 1/\gamma$, $\varepsilon_1 = 0.0001$, and $\varepsilon_2 = 0.001$. Under the present normalization, u_∞ is identical to M_∞. The inviscid counterpart of this problem has previously been treated with $M_\infty = 0.9$ [20]. Therefore, the present calculation also specifies $M_\infty = 0.9$ plus $Pr_\infty = 0.71$ and $Re_\infty = 10$, 100, 1000, and ∞. Again, the numerical settings are given by $\Delta x = \Delta y = 0.05$, while $\Delta t = 0.001$ is selected for DNS, and $\Delta t = 0.00001$ for FDLBM.

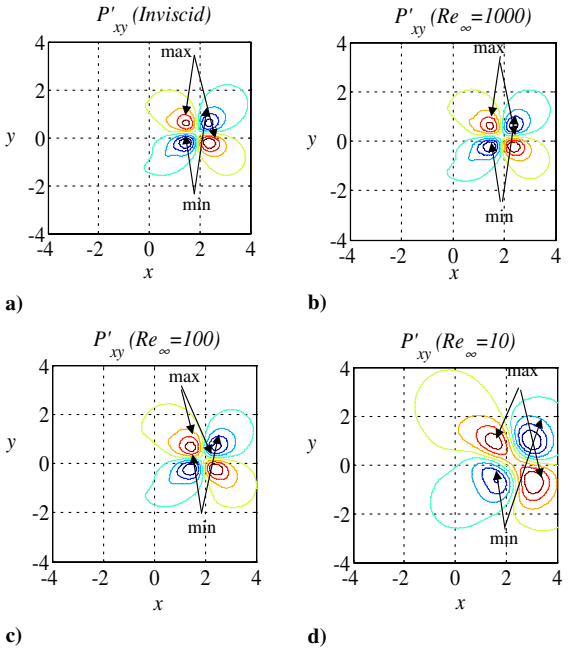

Fig. 4 Contour plots (with eight evenly distributed contour lines) of four different *Re*. The (max, min) for part a is 9.7981e − 005, −9.6920e − 005, for part b is 9.5376e − 005, −9.4783e − 005, for part c is 7.6808e − 005, −7.7825e − 005, and for part d is 3.7115e − 005, −3.8695e − 005. Each panel (a, b, c, and d) is divided into four quadrants. Labeling starts with the upper left quadrant as 1 and the lower left quadrant as 4 in a clockwise fashion. For quadrants a and c, the maximum is located in the innermost contour and decreases outward; for quadrants b and d, the minimum is located in the innermost contour and increases outward.

Only the contours of P'_{xy} are plotted in Fig. 4; other contours are very similar to those reported in [20], therefore, they are not shown. The distributions of u and v, and ρ and p are shown in Figs. 5 and 6, respectively, to illustrate the effects of Re_∞ and the ability of the FDLBM to replicate them compared with DNS results. All Re_∞ cases calculated are plotted in each figure. They illustrate the effects of Re_∞ on the propagation of the pressure pulse and their interaction with the entropy and vorticity pulse. As Re_∞ decreases, the pressure contours become more and more diffuse with similar behavior recorded for P'_{xy} (Fig. 4). Therefore, it plays a major role in the correct calculation of the interaction between the three pulses. As for the distributions of u and v and ρ and p, Re_∞ effects lead to a substantial reduction of the peak values as Re_∞ decreases to 10. In fact, the distributions of $u - u_\infty$ and $p - p_\infty$ are significantly different for $Re_\infty = 100$ and 10 compared with the distributions for the inviscid and $Re_\infty = 1000$ cases (Figs. 5 and 6). All of these results show that the FDLBM solutions are essentially identical to those given by DNS, a claim supported by the error norms tabulated in Table 3. The error norms are at least one order better than those reported in [19] using the same finite difference scheme but a different f_α^{eq}.

C. Shock Structure Problems

Having successfully validated the FDLBM against thermal and aeroacoustics problems, the next task is to validate the FDLBM against shock structure problems. The aim is to demonstrate that the FDLBM can be extended to simulate a more complicated flow model, such as the Brenner–NS model. The ability of the NS equations and the corrections put forward by Brenner [37,38] to replicate shock structure has been investigated previously [42]. It is shown here that the FDLBM suffers the same inadequacy as the NS equations and that the proposed Brenner corrections can be built into the present f_α^{eq}.

1. *Structure of a Steady Plane Shock*

The structure of a steady plane shock is so thin that it challenges the validity of the continuum $Kn \ll 1$ assumption. This is a 1-D boundary value problem. The governing equation is the 1-D steady NS equation, which in dimensionless form is given by

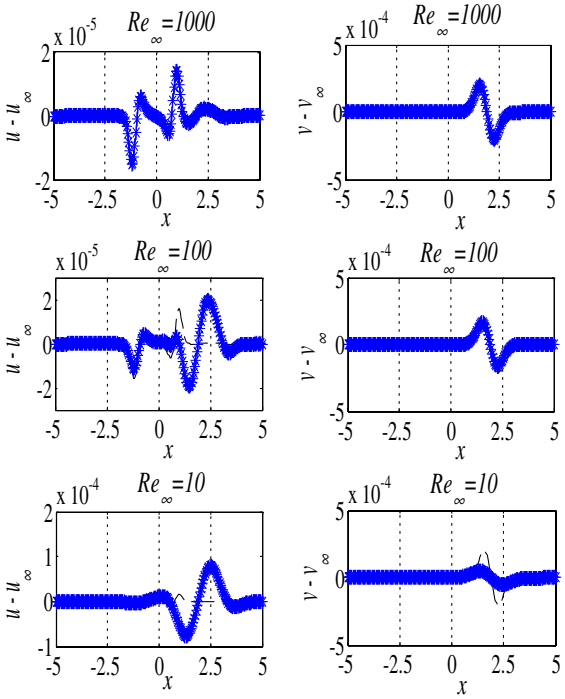

Fig. 5 Distribution of u and v at $t = 1$ for different Re_∞: a) u along x axis, b) v along x axis. The dashed curve is the inviscid solution, the continuous curve represents the DNS results, and the crosses represent the FDLBM results. In these plots, the DNS and FDLBM results essentially overlap each other.

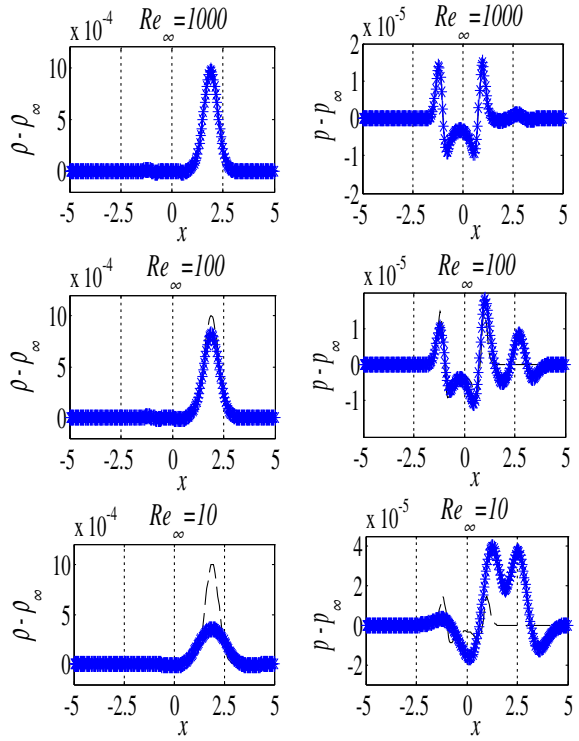

Fig. 6 Distribution of p and ρ at $t = 1$ for different Re_∞ along x axis: a) ρ, b) p. The dashed curve is the inviscid solution, the continuous curve represents the DNS results, and the crosses represent the FDLBM results. In these plots, the DNS and FDLBM results essentially overlap each other.

$$\frac{\partial}{\partial x}(\rho u) = 0 \tag{38a}$$

$$\frac{\partial}{\partial x}\left[p + \rho u^2 - \frac{2\mu M_\infty}{Re_\infty}\frac{\partial u}{\partial x} - \frac{\lambda M_\infty}{Re_\infty}\frac{\partial u}{\partial x}\right] = 0 \tag{38b}$$

$$\frac{\partial}{\partial x}\left[u\left(p + \rho e + \frac{1}{2}\rho u^2\right) - \frac{\kappa\gamma M_\infty}{Re_\infty Pr_\infty}\frac{\partial e}{\partial x} - u\frac{2\mu M_\infty}{Re_\infty}\frac{\partial u}{\partial x} - u\frac{\lambda M_\infty}{Re_\infty}\frac{\partial u}{\partial x}\right] = 0 \tag{38c}$$

where λ is the second coefficient of viscosity. Asymptotically, the shock is bounded by two equilibrium states. The boundary condition is related by the Rankine–Hugoniot condition

Table 3 Error norms comparison between finite difference lattice Boltzmann method and direct numerical simulation results for different Re_∞ of aeroacoustics case: three pulses in uniform stream

Error norms	L_∞	L_2	L_1
	$Re_\infty = 1000$		
p	1.2744e − 007	1.7168e − 008	9.8462e − 009
ρ	1.2478e − 007	1.7390e − 008	1.0199e − 008
u	2.0570e − 007	1.3417e − 008	4.5369e − 009
	$Re_\infty = 100$		
p	1.3607e − 007	1.7868e − 008	1.0128e − 008
ρ	1.4410e − 007	1.8490e − 008	1.0623e − 008
u	1.7995e − 007	1.1879e − 008	4.1203e − 009
	$Re_\infty = 10$		
p	1.0619e − 007	1.6911e − 008	8.8471e − 009
ρ	1.4999e − 007	1.9871e − 008	9.9455e − 009
u	6.6905e − 008	6.4654e − 009	3.0445e − 009

$$\frac{\rho_2}{\rho_1} = \frac{u_1}{u_2} = \frac{(\gamma+1)M_1^2}{2 + (\gamma-1)M_1^2}, \qquad \frac{p_2}{p_1} = 1 + \frac{2\gamma(M_1^2 - 1)}{\gamma + 1} \tag{39}$$

where subscripts 1 and 2 represents the state ahead (upstream) and behind (downstream) the shock, respectively. The state ahead of the shock (state 1) is used as reference. The characteristic length is chosen to be the mean free path, which is given by

$$\hat{L} = \frac{16}{5\sqrt{\pi}}\left(\frac{\hat{\mu}_1}{\hat{\rho}_1\sqrt{2R\hat{T}_1}}\right) \tag{40}$$

where the hat is again used to denote dimensional quantities, $\hat{T}$ is temperature, and R is the universal gas constant. Therefore, Re_∞ is given by

$$Re_\infty = \frac{\hat{\rho}_1\hat{u}_1\hat{L}}{\hat{\mu}_1} = \frac{16}{5\sqrt{2\pi/\gamma}}\left(\frac{\hat{\mu}_1}{\sqrt{\gamma R\hat{T}_1}}\right) = \frac{16}{5\sqrt{2\pi/\gamma}}M_1 \tag{41}$$

and $Pr_\infty = \hat{\mu}_\infty(\hat{c}_p)_\infty/\hat{\kappa}_\infty$. Because it is a steady shock, the shock Mach number is the Mach number ahead of the shock, that is, $M_\infty = M_1$. Power law is used to represent the variation of μ with $\hat{T}$

$$\mu = \frac{\hat{\mu}}{\hat{\mu}_1} = \left(\frac{\hat{T}}{\hat{T}_1}\right)^s = \left(\frac{\hat{p}/\hat{\rho}}{\hat{p}_1/\hat{\rho}_1}\right)^s = \left(\frac{p}{\rho}\frac{\rho_1}{p_1}\right)^s \tag{42}$$

where s is a constant equal to 0.816 and 0.756 for argon and nitrogen gas, respectively. Similar power law given in [2] will also be assumed for the thermal conductivity κ. As for λ, the Stokes hypothesis $\lambda = -2\mu/3$ is assumed, which is suitable for monatomic gas only [43].

The solution of Eqs. (38a–38c) is obtained by solving their unsteady counterparts until a steady-state solution is achieved. The initial condition is given by

$$\rho = \begin{cases} \rho_1 \\ \rho_2 \end{cases}, \qquad u = \begin{cases} u_1 \\ u_2 \end{cases}, \qquad p = \begin{cases} p_1 & \text{for } x < 0 \\ p_2 & \text{for } x \geq 0 \end{cases} \tag{43}$$

A fixed boundary of state 1 at $x \to -\infty$ is set so that

$$\rho_1 = 1, \qquad u_1 = M_1, \qquad p_1 = 1/\gamma \tag{44}$$

while the boundary state 2 at $x \to +\infty$ is set according to the Rankine–Hugoniot condition given in Eq. (39). These numerical settings are similar to those given in [44,45]. The data is presented in the normalized value $\tilde{A}$ defined as

$$\tilde{A} = \frac{A - A_1}{A_2 - A_1} \tag{45}$$

2. *Finite Difference Lattice Boltzmann Method Simulation of Shock Structure*

Altogether three cases are calculated: 1) Ohwada's [46] argon shock at $M_1 = 1.2$, 2) Alsmeyer's [47] argon shock at $M_1 = 1.55$, and 3) Alsmeyer's [47] nitrogen shock at $M_1 = 1.53$. The solutions of Eqs. (38a–38c) and the simulations given by the FDLBM are compared with another numerical result [46] obtained by solving the Boltzmann equation directly, and with experimental measurements [47]. These comparisons are shown in Figs. 7 and 8. Because this is a 1-D shock $P'_{xx} = P'_{xy} = 0$ and the only nonzero component is P'_{yy}, the distribution of P'_{yy} for each shock is also plotted as panel b in each figure. Two observations can be made from these figures. The first is that the present simulations, obtained either from the FDLBM or by solving Eqs. (38a–38c) numerically (DNS), are essentially identical. This is significant because in the calculations of the previous section, the transport coefficients μ and κ are kept constant. However, in the present calculation they are varying nonlinearly with temperature. The excellent agreement between the FDLBM and DNS results shows the validity of the FDLBM. The magnitude and behavior of P'_{yy} follows closely that of the shock profile. This indicates the

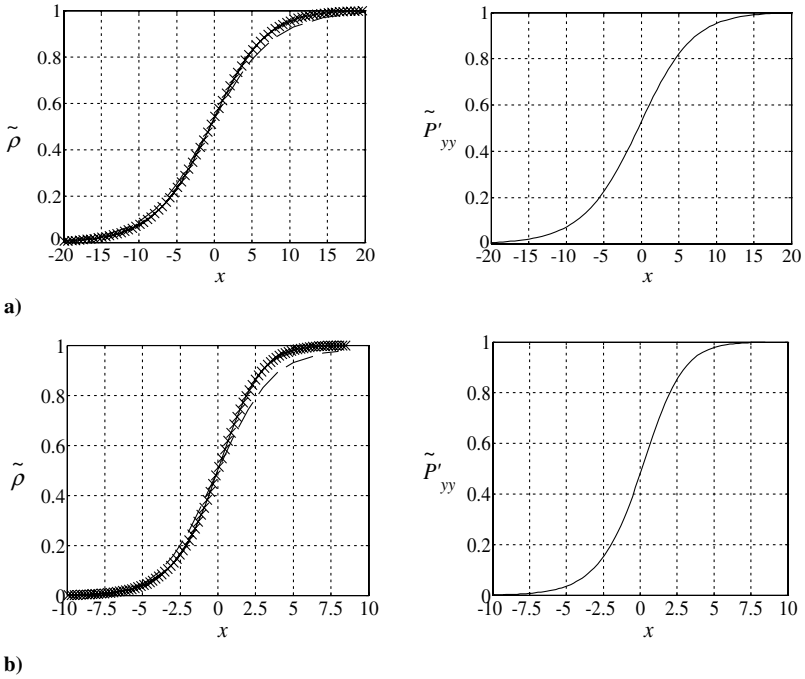

Fig. 7 Shock profile for argon gas with a shock Mach number. In the two top boxes, $M_1 = 1.2$, $\Delta x = 0.5$: a) ρ, b) P''_{yy}, and the dashed line is the numerical result of Ohwada [46]. In the bottom two boxes, $M_1 = 1.55$, $\Delta x = 0.2$: a) ρ, b) P''_{yy}, and the dashed line is the experimental result of Alsmeyer [47]. In both cases, x is the DNS result, the dashed line is the FDLBM result, and $P'_{xx} = P'_{xy} = 0$ for 1-D shock. For these two cases, $Pr_\infty = 2/3$, $\gamma = 5/3$, and $s = 0.816$ are specified.

importance of P'_{ij} in the FDLBM simulation. It could be speculated that if the contribution of P'_{yy} is absent, as in conventional LBM, the simulated shock structure would most likely be incorrect. The second observation is that these results do not quite agree with known numerical data and experimental measurements. The present results are symmetric about $x = 0$, while the numerical result of [46] and experimental measurements of [47] show asymmetry to different degrees depending on whether the gas is argon or nitrogen. The discrepancy between FDLBM (and DNS) results and known data increases from argon to nitrogen shock as the asymmetry becomes more and more acute. This discrepancy is not surprising because the NS equations are subject to the continuum assumption, which is not adequate for shock structure problems.

3. Brenner Correction to Finite Difference Lattice Boltzmann Method Simulation

Macroscopically, a shock wave appears as a discontinuity; however, that is not the case in microscopic dimension. Simulation of the structure of a stationary shock often represents a challenge for models of rarefied gas flow because Kn is no longer small and the continuum assumption is in doubt. Although the concept of a continuum might not be meaningful in shock structure simulation, researchers are not willing to give up the macroscopic approach; they intended to modify the NS equations to achieve an extended thermodynamics model that might be suitable for rarefied gas. Gilbarg and Paolucci [43] explored the consequence and potential of continuum methods to simulate shock structure in detail. Weiss [48] showed by numerical calculation that extended aerodynamic equations developed by the method of moments have restrictions related to M. Continuous shock structure only exists up to a critical M, e.g., no continuous shock exists beyond $M_c = 1.65$ even after invoking Grad's 13-moment theory. Recently, Brenner [37,38] proposed modifications to the NS equations that are based on theoretical arguments. It is hypothesized that the velocity appearing in the velocity gradient term in Newton's rheological law should be changed from the fluid's mass-based velocity to its volume-based velocity. Because the proposal has supporting experimental evidence, discernible improvement for the shock structure is obtained if these modified equations were solved rather than the NS equations. The normalized NS equations with Brenner's correction [37,38] are given by

$$\frac{\partial \rho}{\partial t} + \frac{\partial}{\partial x_j}(\rho u_j) = 0 \tag{46a}$$

$$\frac{\partial (\rho u_i)}{\partial t} + \frac{\partial}{\partial x_j}[p\delta_{ij} + \rho u_i u_j - \Im_{ij}] = 0 \tag{46b}$$

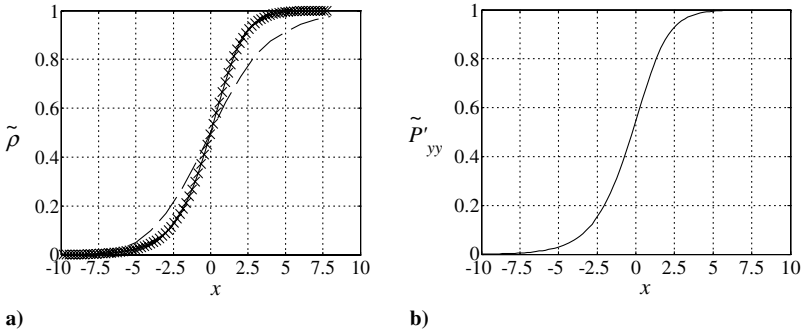

Fig. 8 Shock profile for nitrogen gas with a shock Mach number $M_1 = 1.53$: a) ρ, and b) P''_{yy}. The dashed line is the experimental result of Alsmeyer [47], x is the current DNS result, and the solid line is the FDLBM result. For this 1-D shock, $P'_{xx} = P'_{xy} = 0$ and $Pr_\infty = 0.71$, $\gamma = 1.4$, $s = 0.756$, and $\Delta x = 0.2$ are specified.

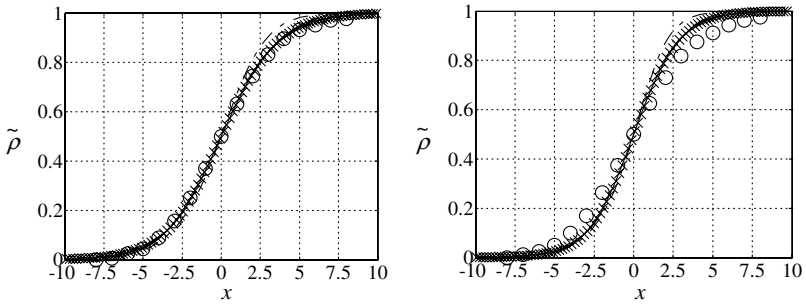

Fig. 9 Shock structure simulation and its comparison with experimental and DNS results: a) argon gas at $M_1 = 1.55$, and b) nitrogen gas at $M_1 = 1.53$. The dashed dot line represents numerical simulation of NS equations, the dashed line represents DNS of NS equations with Brenner correction [37,38]; x represents FDLBM with Brenner correction [37,38], and the circle represents measurements [47]. In these calculations, $Pr_b = 1$ and $\Delta x = 0.2$.

$$\frac{\partial}{\partial t}\left(\rho e + \frac{1}{2}\rho|\boldsymbol{u}|^2\right) + \frac{\partial}{\partial x_j}\left[u_j\left(p + \rho e + \frac{1}{2}\rho|\boldsymbol{u}|^2\right) - u_k\Im_{jk} - \frac{\gamma M_\infty \kappa}{Pr_\infty Re_\infty}\frac{\partial e}{\partial x_j} - \frac{M_\infty}{(Pr_b)_\infty Re_\infty}\frac{\mu p}{\rho^2}\frac{\partial \rho}{\partial x_j}\right] = 0 \tag{46c}$$

where the stress tensor $\Im_{ij}$ is modified by adding an additional term B_{ij}, such that

$$\Im_{ij} = \frac{\mu M_\infty}{Re_\infty}\left(\frac{\partial u_j}{\partial x_i} + \frac{\partial u_i}{\partial x_j}\right) + \frac{\lambda M_\infty}{Re_\infty}\left(\frac{\partial u_k}{\partial x_k}\right)\delta_{ij} + B_{ij} \tag{47a}$$

$$B_{ij} = \left[\frac{2\mu M_\infty^2}{Re_\infty^2 (Pr_b)_\infty}\frac{\partial}{\partial x_i}\left(\frac{\mu}{\rho^2}\frac{\partial \rho}{\partial x_j}\right)\right] \tag{47b}$$

and the square bracketed term is defined as

$$[A] \equiv A'' - ((1/3)tr(A'')I, \qquad A'' = (A + A^T)/2 \tag{47c}$$

The parameter Pr_b is defined as the ratio of the kinematic viscosity to the volume diffusivity coefficient [42,43]. As suggested in [42], Pr_b should be greater than or equal to unity to avoid nonphysical behavior. Power law variation of μ and κ with T can again be assumed, and $\lambda = -2\mu/3$ can be invoked.

In view of the similarity between Eqs. (1–3) and (46a–46c), it is worthy to investigate the extension of the FDLBM to include the Brenner–NS model [42] to see if the same improvements can be obtained. The Brenner–NS model is given by Eqs. (46a–46c). Similarly, the FDLBM could be modified by requiring the modeled BE to recover Eqs. (46a–46c) with $\Im_{ij}$ given by Eq. (47a). The procedure is identical to that given above for the recovery of the NS equations and can again be deduced by following the procedure outlined in Sec. III. Therefore, the derivation details are omitted here. Only the simulation results for the argon shock at $M_1 = 1.55$ and the nitrogen shock at $M_1 = 1.53$ are shown in Fig. 9. The plots of P'_{yy} are essentially similar to those shown in Figs. 7 and 8; therefore, they are not plotted in Fig. 9. In these figures, four sets of data are shown. They are the measurements of [47], numerical simulation of the Brenner–NS model, numerical simulation of the FDLBM with the Brenner correction, and finally numerical simulation of the NS equations with no Brenner correction.

For the argon shock, Brenner's correction is sufficient to bring the simulation results to agree with measurements (Fig. 9a). In other words, for monatomic gas, Brenner's correction is sufficient to model the collision behavior of the gas particles to allow an extension of the small Kn assumption to predict shock structure up to $M_1 = 1.55$. The same correction proves to be inadequate for a diatomic gas (Fig. 9b) at essentially the same M_1. This shows that the extension of the continuum assumption to high M flow of nonequilibrium compressible flow is not as applicable. Nevertheless, the FDLBM results are identical to those given by the Brenner–NS model simulation (DNS). This shows that the FDLBM correctly recovers the continuum NS equations and their Brenner modification. In view of these results, the FDLBM can be extended to treat models with nonlinear transport coefficients, and an extended thermodynamics model such as the Brenner–NS model.

VII. Conclusions

A BGK-type modeled Boltzmann equation based on an alternative equilibrium particle distribution function is proposed. The coefficients in the proposed equilibrium distribution function are determined by invoking constraints derived not just from the macrofluid properties, but also from the NS equations. Consequently, it allows the NS equations to be recovered identically from a first-order expansion of the distribution function, rather than resorting to the second-order expansion like other conventional BGK-type modeled Boltzmann equation. However, the formulation cannot recover the transport coefficients of the fluid because one stipulation has to be made and that is Re_∞, Pr_∞, and M_∞ have to be specified, much like in the dimensionless NS equations where these nondimensional numbers are assumed known.

The improved BGK-type modeled Boltzmann equation is resolved assuming a velocity lattice at each grid point of a finite difference scheme. This scheme is designated as FDLBM and incorporates a splitting method to numerically solve the lattice equations. For two-dimensional problems, only a nine-velocity lattice model is required. Validations are carried out against benchmark thermal and aeroacoustics problems, and 1-D structures of argon and nitrogen shocks. Excellent agreement between the FDLBM results and those obtained either analytically or from DNS of the NS equations has been achieved for all thermal and aeroacoustics problems investigated. In the shock structure problems attempted, it is found that the FDLBM solutions with and without the Brenner correction are in perfect agreement with those obtained from DNS of the continuum NS equations, and its Brenner modification. Therefore, the FDLBM can be extended to treat models with nonlinear transport coefficients, and with an extended thermodynamics model, such as the Brenner-NS model.

Appendix A: Determination of the Boundary Constants for P'_{ij}

The boundary constants can be determined as follows. Equation (28) implies that on the left and right boundaries the y derivative of P'_{xy} vanishes. Similarly, Eq. (29) implies that on the top and bottom boundaries the x derivative of P'_{xx} vanishes. Therefore, combining Eqs. (27) and (30) ensures that Eq. (23a) is satisfied on all four boundaries. Taking the derivative of Eq. (23a) with respect to x, and using Eq. (26), the following equation is obtained

$$\frac{\partial^2 P'_{xy}}{\partial x \partial y} + \frac{\partial^2 P'_{yy}}{\partial^2 y} = 0 \tag{A1a}$$

Similarly, taking the derivative of Eq. (23a) with respect to y, and using Eq. (24) yields

$$\frac{\partial^2 P'_{xy}}{\partial^2 x} + \frac{\partial^2 P'_{yy}}{\partial x \partial y} = 0 \tag{A1b}$$

This means that on the boundary Eqs. (A1a) and (A1b) must be satisfied simultaneously; the result is

$$\frac{\partial P'_{xy}}{\partial x} + \frac{\partial P'_{yy}}{\partial y} = k \tag{A1c}$$

where k is an arbitrary constant. Therefore, Eq. (A1c) holds on all four boundaries, which is a weaker condition compared with Eq. (23b).

It can be shown that using the above proposed boundary conditions, solving Eqs. (23c), (24), and (26) is equivalent to solving a weaker system of equations, Eqs. (23a), (A1a), and (23c), in the entire domain. Taking the derivative of Eq. (24) with respect to y, that of Eq. (26) with respect to x, and then summing up gives

$$\left(\frac{\partial^2}{\partial x^2} + \frac{\partial^2}{\partial y^2}\right)\left(\frac{\partial P'_{xx}}{\partial x} + \frac{\partial P'_{xy}}{\partial y}\right) = 0 \tag{A2}$$

which is the Laplacian of the LHS of Eq. (23a). Consequently, Eq. (23a) is satisfied along the boundary and the whole domain ($\because \nabla^2 u = 0 \& u|_{\text{bdy}} = 0 \Leftrightarrow u \equiv 0$). Using Eq. (23c) and a similar technique as that given above leads to

$$\left(\frac{\partial^2}{\partial x^2} + \frac{\partial^2}{\partial y^2}\right)\left(\frac{\partial P'_{xy}}{\partial x} + \frac{\partial P'_{yy}}{\partial y}\right) = 0 \tag{A3}$$

Similarly, Eq. (A1c) is satisfied along the boundary; therefore, due to Eq. (A3), Eq. (A1c) is satisfied in the entire domain (by the maximum principle for Laplace equation).

The weaker system of equations [Eqs. (23a), (23c), and (A1c)] is different from the original system [Eqs. (23a–23c)]; thus implying that the constant k in Eq. (A1c) might not be zero. If the weaker system were to return to the original system, k has to be zero. To find the condition under which this is true, double integrate Eq. (A1c) along x and y to give

$$\begin{aligned}
&\int_0^H \int_0^L \left[\frac{\partial P'_{xy}}{\partial x} - \frac{\partial P'_{xx}}{\partial y} + \frac{\partial A}{\partial y} = k\right] \mathrm{d}x\mathrm{d}y \\
&\quad \Rightarrow \int_0^H \int_0^L \frac{\partial P'_{xy}}{\partial x}\,\mathrm{d}x\mathrm{d}y - \int_0^L \int_0^H \frac{\partial P'_{xx}}{\partial y}\,\mathrm{d}y\mathrm{d}x \\
&\qquad + \int_0^L \int_0^H \frac{\partial A}{\partial y}\,\mathrm{d}y\mathrm{d}x = kLH \\
&\quad \Rightarrow \int_0^H P'_{xy}|_{x=L} - P'_{xy}|_{x=0}\,\mathrm{d}y - \int_0^L P'_{xx}|_{y=H} - P'_{xx}|_{y=0}\,\mathrm{d}x \\
&\qquad + \int_0^L A|_{y=H} - A|_{y=0}\,\mathrm{d}x = kLH \\
&\quad \Rightarrow (k_{1R} - k_{1L})H - (k_{2T} - k_{2B})L + \int_0^L A|_{y=H} \\
&\qquad - A|_{y=0}\,\mathrm{d}x = kLH
\end{aligned} \tag{A4}$$

Equation (A4) shows that one of the simplest condition for which $k = 0$ can be achieved is

$$k_{1R} = k_{1L} = k_{2B} = 0, \qquad k_{2T} = \frac{1}{L}\int_0^L (A|_{y=H} - A|_{y=0})\,\mathrm{d}x \tag{A5}$$

Therefore, Eq. (A5) provides the boundary constants for the solution of Eqs. (23a–23c).

Acknowledgments

The authors would like to acknowledge support from the Research Grants Council of the Government of the Hong Kong Special Administrative Region given them under grant numbers PolyU1/02C, PolyU5303/03E and PolyU5272/04E. RMCS further acknowledges support received as Co-PI from the NSF Grant CBET-0854411 awarded to New Mexico State University.

References

[1] Bhatnagar, P. L., Gross, E. P., and Kok, M., "A Model for Collision Processes in Gases: I. Small Amplitude Processes in Charged and Neutral One-Component Systems," *Physical Review*, Vol. 94, No. 3, 1954, pp. 511–525. doi:10.1103/PhysRev.94.511

[2] Chapman, S., and Cowling, T. G., *The Mathematical Theory of Nonuniform Gases*, 3rd ed., Cambridge Univ. Press, Cambridge, England, 1990.

[3] Broadwell, J. E., "Study of Rarefied Shear Flow by the Discrete Velocity Method," *Journal of Fluid Mechanics*, Vol. 19, No. 3, 1964, pp. 401–414. doi:10.1017/S0022112064000817

[4] Wolf-Gladrow, D. A., *Lattice-Gas Cellular Automata and Lattice Boltzmann Models*, Springer–Verlag, New York, 2000, Chap. 5.

[5] Cao, N. S., Chen, S., Jin, S., and Martinez, D., "Physical Symmetry and Lattice Symmetry in the Lattice Boltzmann Method," *Physical Review E: Statistical Physics, Plasmas, Fluids, and Related Interdisciplinary Topics*, Vol. 55, 1997, pp. R21-24. doi:10.1103/PhysRevE.55.R21

[6] Mei, R., and Shyy, W., "On the Finite Difference-Based Lattice Boltzmann Method in Curvilinear Coordinates," *Journal of Computational Physics*, Vol. 143, No. 2, 1998, pp. 426–448. doi:10.1006/jcph.1998.5984

[7] Chen, S., and Doolen, G. D., "Lattice Boltzmann Method for Fluid Flows," *Annual Review of Fluid Mechanics*, Vol. 30, No. 1, 1998, pp. 329–364. doi:10.1146/annurev.fluid.30.1.329

[8] Wellein, G., Lammers, P., Hager, G., Donath, S., and Zeiser, T., "Towards Optimal Performance for Lattice Boltzmann Applications on Terascale Computers," *Parallel Computational Fluid Dynamics: Theory and Applications*, edited by A. Deane, G. Brenner, D. Emerson, J. McDonough, and D. Tromeur-Dervout, Proceedings of the 2005 International Conference on Parallel Computational Fluid Dynamics, Elsevier, New York, May 2005, pp. 31–40.

[9] Wellein, G., Zeiser, T., Hager, G., and Donath S., "On the Single Processor Performance for Simple Lattice Boltzmann Kernels," *Computers and Fluids*, Vol. 35, Nos. 8–9, 2006, pp. 910–919. doi:10.1016/j.compfluid.2005.02.008

[10] McNamara, G., and Zanetti, G., "Use of the Boltzmann Equation to Simulate Lattice-Gas Automata," *Physical Review Letters*, Vol. 61, No. 20, 1988, pp. 2332–2335. doi:10.1103/PhysRevLett.61.2332

[11] He, X., and Luo, L. S., "Lattice Boltzmann Model for the Incompressible Navier–Stokes Equation," *Journal of Statistical Physics*, Vol. 88, Nos. 3–4, 1997, pp. 927–944. doi:10.1023/B:JOSS.0000015179.12689.e4

[12] Alexander, F. J., Chen, S., and Sterling, J. D., "Lattice Boltzmann Thermohydrodynamics," *Physical Review E: Statistical Physics, Plasmas, Fluids, and Related Interdisciplinary Topics*, Vol. 47, No. 4, 1993, pp. R2249–R2252. doi:10.1103/PhysRevE.47.R2249

[13] McNamara, G., and Alder, B., "Analysis of the Lattice Boltzmann Treatment of Hydrodynamics," *Physica A: Statistical Mechanics and its Applications*, Vol. 194, Nos. 1–4, 1993, pp. 218–228. doi:10.1016/0378-4371(93)90356-9

[14] Chen, Y., Ohashi, H., and Akiyama, M., "Thermal Lattice Bhatnagar–Cross–Krook Model Without Nonlinear Deviations in Macrodynamic Equations," *Physical Review E: Statistical Physics, Plasmas, Fluids, and Related Interdisciplinary Topics)*, Vol. 50, No. 4, 1994, pp. 2776–2783. doi:10.1103/PhysRevE.50.2776

[15] Kataoka, T., and Tsutahara, M., "Lattice Boltzmann Model for the Compressible Navier–Stokes Equations with Flexible Specific-Heat Ratio," *Physical Review E: Statistical Physics, Plasmas, Fluids, and Related Interdisciplinary Topics)*, Vol. 69, No. 3, 2004, p. 035701. doi:10.1103/PhysRevE.69.035701

[16] Hu, S., Yan, G., and Shi, W., "A Lattice Boltzmann Model for Compressible Perfect Gas," *Acta Mechanica Sinica (English Edition)*, Vol. 13, No. 3, 1997, pp. 218–226.

[17] Tsutahara, M., Kataoka, T., Takada, N., Kang, H. K., and Kurita, M., "Simulations of Compressible Flows by Using the Lattice

Boltzmann and the Finite Difference Lattice Boltzmann Methods," *Computational Fluid Dynamics Journal*, Vol. 11, No. 1, 2002, pp. 486–493.

[18] Li, Q., He, Y. L., Wang, Y., and Tao, W. Q., "Coupled Double-Distribution-Function Lattice Boltzmann Method for the Compressible Navier–Stokes Equations," *Physical Review E: Statistical Physics, Plasmas, Fluids, and Related Interdisciplinary Topics*, Vol. 76, 2007. doi:10-1103/PhysRevE.76.056703

[19] Li, X. M., Leung, R. C. K., and So, R. M. C., "One-Step Aeroacoustics Simulation Using Lattice Boltzmann Method," *AIAA Journal*, Vol. 44, No. 1, 2006, pp. 78–89. doi:10.2514/1.15993

[20] Fu, S. C., So, R. M. C., and Leung, R. C. K., "Modeled Boltzmann Equation and its Application to Direct Aeroacoustics Simulation," *AIAA Journal*, Vol. 46, No. 7, 2008, pp. 1651–1662. doi:10.2514/1.33250

[21] So, R. M. C., Leung, R. C. K., and Fu, S. C., "Modeled Boltzmann Equation and its Application to Shock Capturing Simulation," *AIAA Journal*, Vol. 46, No. 12, 2008, pp. 3038–3048. doi:10.2514/1.35332

[22] Watari, M., "Finite Difference Lattice Boltzmann Method with Arbitrary Specific Heat Ratio Applicable to Supersonic Flow Simulations," *Physica A: Statistical Mechanics and its Applications*, Vol. 382, No. 2, 2007, pp. 502–522. doi:10.1016/j.physa.2007.03.037

[23] Watari, M., and Tsutahara, M., "Supersonic Flow Simulations by a Three-Dimensional Multispeed Thermal Model of the Finite Difference Lattice Boltzmann Method," *Physica A: Statistical Mechanics and its Applications*, Vol. 364, No. , 2006, pp. 129–144. doi:10.1016/j.physa.2005.06.103

[24] Yan, G., Chen, Y., and Hu, S., "Simple Lattice Boltzmann Model for Simulating Flows with Shock Wave," *Physical Review E: Statistical Physics, Plasmas, Fluids, and Related Interdisciplinary Topics*, Vol. 59, No. 1, 1999, pp. 454–459. doi:10.1103/PhysRevE.59.454

[25] Kataoka, T., and Tsutahara, M., "Lattice Boltzmann Method for the Compressible Euler Equations," *Physical Review E: Statistical Physics, Plasmas, Fluids, and Related Interdisciplinary Topics*, Vol. 69, No. 5, 2004, p. 056702. doi:10.1103/PhysRevE.69.056702

[26] McNamara, G. R., Garcia, A. L., and Alder, B. J., "Stabilization of Thermal Lattice Boltzmann Models," *Journal of Statistical Physics*, Vol. 81, Nos. 1–2, 1995, pp. 395–408. doi:10.1007/BF02179986

[27] Teixeira, C., Chen, H., and Freed, D. M., "Multi-Speed Thermal Lattice Boltzmann Method Stabilization via Equilibrium Under-Relaxation," *Computer Physics Communications*, Vol. 129, Nos. 1–3, 2000, pp. 207–226. doi:10.1016/S0010-4655(00)00108-9

[28] Lallemand, P., and Luo, L. S., "Theory of the Lattice Boltzmann Method: Acoustic and Thermal Properties in Two and Three Dimensions," *Physical Review E: Statistical Physics, Plasmas, Fluids, and Related Interdisciplinary Topics*, Vol. 68, No. 3, 2003. doi:10.1103/PhysRevE.68.036706

[29] Lim, C. Y., Shu, C., Niu, X. D., and Chew, Y. T., "Application of Lattice Boltzmann Method to Simulate Microchannel Flows," *Physics of Fluids*, Vol. 14, No. 7, 2002, pp. 2299–2308. doi:10.1063/1.1483841

[30] Lele, S. K., "Direct Numerical Simulations of Compressible Turbulent Flows: Fundamentals and Applications," *Transition, Turbulence and Combustion Modeling*, edited by A. Hanifi, P. F. Alfredsson, A. V. Johansson, , and D. S. Hennigson, Kluwer Academic, Norwell, MA, Chap. 7, 1998, pp. 424–429.

[31] Lele, S. K., "Compact Finite Schemes with Spectral-Like Resolution," *Journal of Computational Physics*, Vol. 103, 1992, pp. 16–42.

[32] Toro, E. F., *Riemann Solvers and Numerical Methods for Fluid Dynamics: A Practical Introduction*, 2nd ed., Springer–Verlag, Berlin, 1999, Chap. 15. doi:10.1016/0021-9991(92)90324-R

[33] Kam, E. W. S., So, R. M. C., and Leung, R. C. K., "Lattice Boltzmann Method Simulation of Aeroacoustics and Nonreflecting Boundary Conditions," *AIAA Journal*, Vol. 45, No. 7, 2007, pp. 1703–1712. doi:10.2514/1.27632

[34] Li, X. M., So, R. M. C., and Leung, R. C. K., "Propagation Speed, Internal Energy and Direct Aeroacoustics Simulation Using Lattice Boltzmann Method," *AIAA Journal*, Vol. 44, No. 12, 2006, pp. 2896–2903. doi:10.2514/1.18933

[35] Gaitonde, D. V., and Visbal, M. R., "Further Development of a Navier–Stokes Solution Procedure Based on Higher-Order Formulas," AIAA Paper 99-0557, 1999.

[36] Visbal, M. R., and Gaitonde, D. V., "Very High-Order Spatially Implicit Schemes for Computational Acoustics on Curvilinear Meshes," *Journal of Computational Acoustics*, Vol. 9, 2001, pp. 1259–1286.

[37] Brenner, H., "Kinematics of volume transport," *Physica A: Statistical Mechanics and Its Applications*, Vol. 349, Nos. 1–2, 2005, pp. 11–59. doi:10.1016/j.physa.2004.10.033

[38] Brenner, H., "Navier–Stokes Revisited," *Physica A: Statistical Mechanics and its Applications*, Vol. 349, Nos. 1–2, 2005, pp. 60–132. doi:10.1016/j.physa.2004.10.034

[39] Visbal, M. R., and Gaitonde, D. V., "High-Order-Accurate Methods for Complex Unsteady Subsonic Flows," *AIAA Journal*, Vol. 37, No. 10, 1999, pp. 1231–1239. doi:10.2514/2.591

[40] Leung, R. C. K., Li, X. M., and So, R. M. C., "Comparative Study of Nonreflecting Boundary Condition for One-Step Duct Aeroacoustic Simulation," *AIAA Journal*, Vol. 44, No. 3, 2006, pp. 664–667. doi:10.2514/1.18215

[41] Tam, C. K. W., and Webb, J. C., "Dispersion-Relation-Preserving Finite Difference Schemes for Computational Aeroacoustics," *Journal of Computational Physics*, Vol. 107, No. 2, 1993, pp. 262–281. doi:10.1006/jcph.1993.1142

[42] Greenshields, C. J., and Reese, J. M., "The Structure of Shock Waves as a Test of Brenner's Modifications to the Navier–Stokes Equations," *Journal of Fluid Mechanics*, Vol. 580, 2007, pp. 407–429.

[43] Gilbarg, D., and Paolucci, D., "The Structure of Shock Waves in the Continuum Theory of Fluids," *Journal of Rational Mechanics and Analysis*, Vol. 2, 1953, pp. 617–642. doi:10.1017/S0022112007005575

[44] Elizarova, T. G., Shirokov, I. A., and Montero, S., "Numerical Simulation of Shock-Wave Structure for Argon and Helium," *Physics of Fluids*, Vol. 17, No. 6, 2005, p. 068101. doi:10.1063/1.1921267

[45] Elizarova, T. G., Shirokov, I. A., and Montero, S., "Numerical Simulation of Shock Wave Structure in Nitrogen," *Physics of Fluids*, Vol. 19, No. 6, 2007, p. 068102. doi:10.1063/1.1921267

[46] Ohwada, T., "Structure of Normal Shock Waves: Direct Numerical Analysis of the Boltzmann Equation for Hard-Sphere Molecules," *Physics of Fluids*, Vol. 5, No. 1, 1993, pp. 217–234. doi:10.1063/1.2738606

[47] Alsmeyer, H., "Density Profiles in Argon and Nitrogen Shock Waves Measured by the Absorption of an Electron Beam," *Journal of Fluid Mechanics*, Vol. 74, No. , 1976, pp. 497–513.

[48] Weiss, W., "Continuous Shock Structure in Extended Thermodynamics," *Physical Review E: Statistical Physics, Plasmas, Fluids, and Related Interdisciplinary Topics*, Vol. 52, No. 6, 1995, pp. R5760-5763. doi:10.1017/S0022112076001912

J. Gore
Associate Editor